

www.acsnano.org

In Situ Oxidation Studies of High-Entropy Alloy Nanoparticles

Boao Song, Yong Yang, Muztoba Rabbani, Timothy T. Yang, Kun He, Xiaobing Hu, Yifei Yuan, Pankaj Ghildiyal, Vinayak P. Dravid, Michael R. Zachariah,* Wissam A. Saidi,* Yuzi Liu,* and Reza Shahbazian-Yassar*



Cite This: ACS Nano 2020, 14, 15131–15143



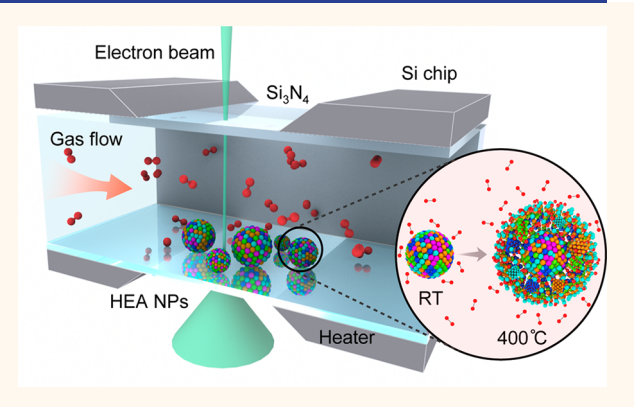
ACCESS

Metrics & More

Article Recommendations

Supporting Information

ABSTRACT: Although high-entropy alloys (HEAs) have shown tremendous potential for elevated temperature, anticorrosion, and catalysis applications, little is known on how HEA materials behave under complex service environments. Herein, we studied the high-temperature oxidation behavior of Fe_{0.28}Co_{0.21}Ni_{0.20}Cu_{0.08}Pt_{0.23}HEA nanoparticles (NPs) in an atmospheric pressure dry air environment by in situ gas-cell transmission electron microscopy. It is found that the oxidation of HEA NPs is governed by Kirkendall effects with logarithmic oxidation rates rather than parabolic as predicted by Wagner's theory. Further, the HEA NPs are found to oxidize at a significantly slower rate compared to monometallic NPs. The outward diffusion of transition metals and formation of disordered oxide layer are observed in real time and confirmed through analytical energy dispersive spectroscopy, and electron energy loss



spectroscopy characterizations. Localized ordered lattices are identified in the oxide, suggesting the formation of Fe₂O₃, CoO, NiO, and CuO crystallites in an overall disordered matrix. Hybrid Monte Carlo and molecular dynamics simulations based on first-principles energies and forces support these findings and show that the oxidation drives surface segregation of Fe, Co, Ni, and Cu, while Pt stays in the core region. The present work offers key insights into how HEA NPs behave under high-temperature oxidizing environment and sheds light on future design of highly stable alloys under complex service conditions.

KEYWORDS: high-entropy alloys, nanoparticles, in situ transmission electron microscopy, oxidation, phase segregation, Kirkendall

igh-entropy alloys, an emerging alloy compound involving five or more principle elements in the form of homogeneous mixed disordered solid solutions, are attracting increased attention because of their superior properties compared to conventional alloys including high mechanical strength, high thermal stability, and better corrosion resistance. 1-4 The successful fabrication of such HEAs has emerged rapidly over the last two decades involving bulk melting, 5,6 solidstate processing,^{7–9} physical vapor deposition,¹⁰ and additive manufacturing.^{11–13} Notably, the lately developed carbothermal shock method¹⁴ allows incorporating multiple metal elements into single-phase HEA NPs and thus provides wide possible applications in catalysis, electronics, structural alloys, and so forth. Further, the recently developed scalable aerosol synthesis 15 method takes a further step toward production of HEA NPs in bulk manufacturing quantities with full potential for industrial applications.

Similar to conventional alloys, industrial service environments for HEAs usually involve critical conditions such as exposure to high-temperature and oxidizing/reducing gases and acidic and

chloride-containing solutions.¹⁶ Several studies have been devoted to understand the corrosion behaviors of HEAs such as oxidation in air^{17–21} and oxygen-containing atmospheres.²² Although most HEAs show single-stage parabolic oxidation kinetics such as FeCoNiCr-based quinary systems at 700–900 °C, ¹⁸ AlCoCrCuFeNi at 800 °C, ¹⁷ and Al_x(NiCoCrFe)_{1-x} at 1050 °C, ¹⁹ two-stage linear and parabolic kinetics can be observed for FeCoNiCrMn HEA below 900 °C. ^{20,22} Composition-dependent multiple oxidation scales were formed in HEA oxides in either layer-to-layer ^{17,18,22} or precipitation ¹⁹ mechanisms. However, these studies are focused on bulk HEAs, and there is still very limited knowledge of how HEA NPs behave

Received: June 24, 2020 Accepted: October 12, 2020 Published: October 20, 2020





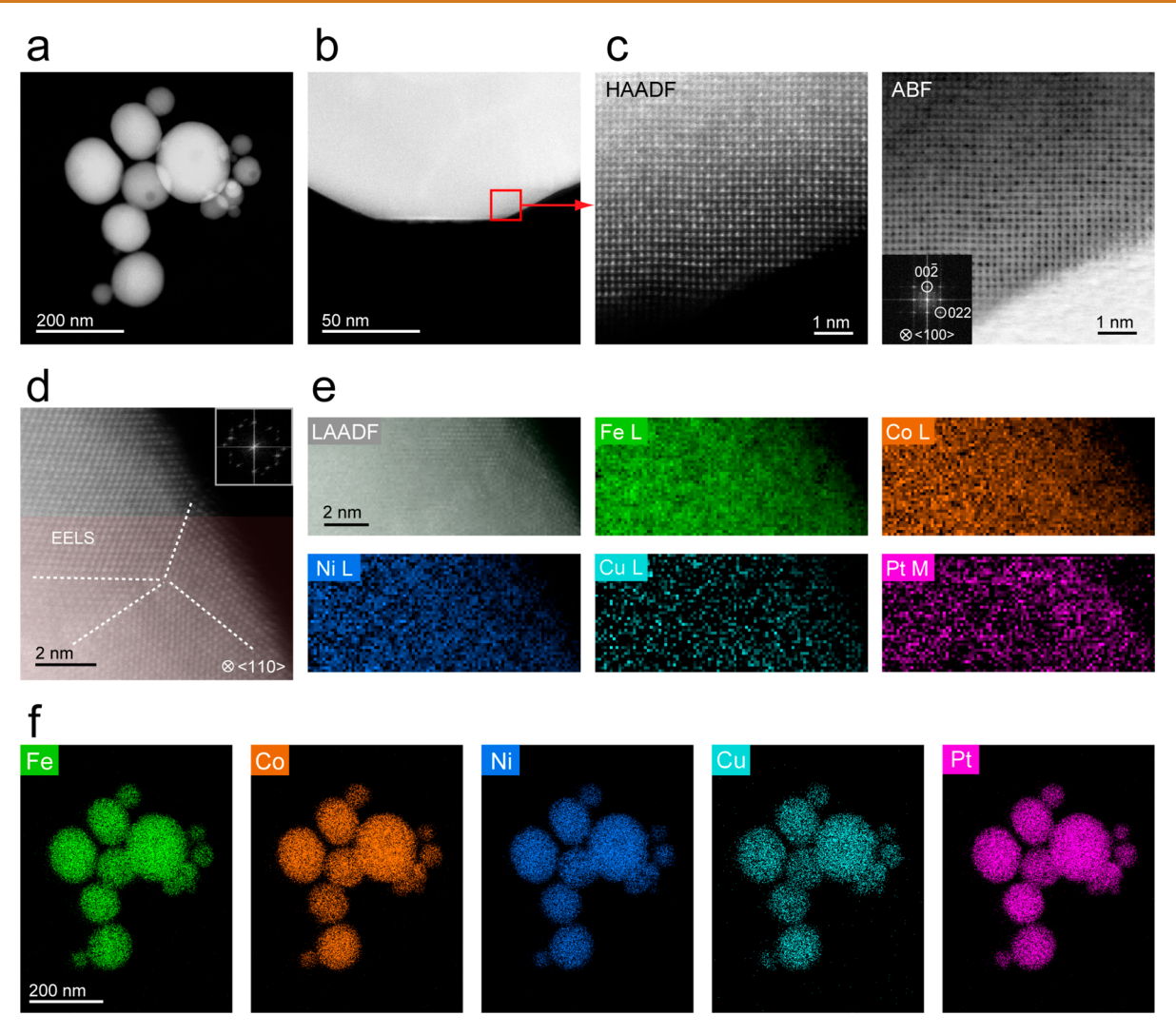


Figure 1. Atomic structure and chemical characterization of HEA NPs. (a) HAADF image showing the as-synthesized HEA NPs. (b) LAADF image focusing on the edge of an individual HEA NP. (c) HAADF and ABF images from the boxed region in (b), showing the atomic structure of HEA in the $\langle 100 \rangle$ zone axis. The inset in the ABF image is the corresponding FFT with highlighted diffraction spots from $\langle 100 \rangle$ planes. (d) LAADF image of HEA in $\langle 110 \rangle$ zone axis with twining marked with dashed lines. The inset shows the corresponding FFT with multiple diffraction spots from twining. Red shadowed region marks the EELS mappings area. (e) EELS mappings from region in (d). Signals are extracted from *L*-edges of Fe, Co, Ni, and Cu and *M*-edge of Pt. (f) EDS mappings of the HEA NPs in (a).

under such environments. One of the key challenges for such nanometer-size HEA NPs is in obtaining structural and compositional information at high spatial and temporal resolution, which requires advanced characterization techniques including transmission electron microscopy (TEM). Recently, the development of in situ open-cell²³⁻²⁷ and closed-cell²⁸⁻³³ environmental TEM with the capability of exposing samples to atmospheric pressure gas environments provides the possibility to study materials behavior under realistic application conditions in real-time. Previous studies have shown that the materials' behavior under redox reactions can be captured including facet evolution of Pt NPs³³ and PdCu,³⁰ phase segregation in bimetallic Pt-Ni³² and PdCu NPs, ²⁸ sintering of Co³¹ and Pt, and core-shell NPs. ³⁴ Benefiting from the *in situ* gas-cell TEM, we studied the high-temperature oxidation behavior of $Fe_{0.28}Co_{0.21}Ni_{0.20}Cu_{0.08}Pt_{0.23}HEA$ NPs in an atmospheric pressure air environment. The structural and compositional evolutions during oxidation at 400 °C are captured in real-time through (scanning) transmission electron microscopy (S)TEM imaging and energy dispersive spectroscopy (EDS)/electron energy loss spectroscopy (EELS) analyses. It is found that the HEA NPs' oxidation kinetics are governed by logarithmic rate constants and are guided by the Kirkendall effect involving outward diffusion of transition metals including Fe, Co, Ni, and Cu. Anisotropic oxidation is observed on adjacent HEA NPs such that oxide prefers to initiate at their connecting interface. The oxide layer is found to have a disordered mixture of Fe₂O₃, CoO, NiO, and CuO crystallites in their Fe³⁺, Co²⁺, Ni²⁺, and Cu²⁺ oxidation states. Hybrid Monte Carlo (MC)/molecular dynamics (MD) simulations based on first-principles calculations support these findings and show that under oxidizing conditions there is a preferential surface segregation of Fe, Co, Ni, and Cu, while Pt remains in the core of the NP.

RESULTS AND DISCUSSION

In the first step, the atomic ordering and chemical composition of the as-synthesized HEA NPs were studied. The NPs were prepared *via* aerosol synthesis method as reported in our earlier work. ¹⁵ The morphology and chemical composition of

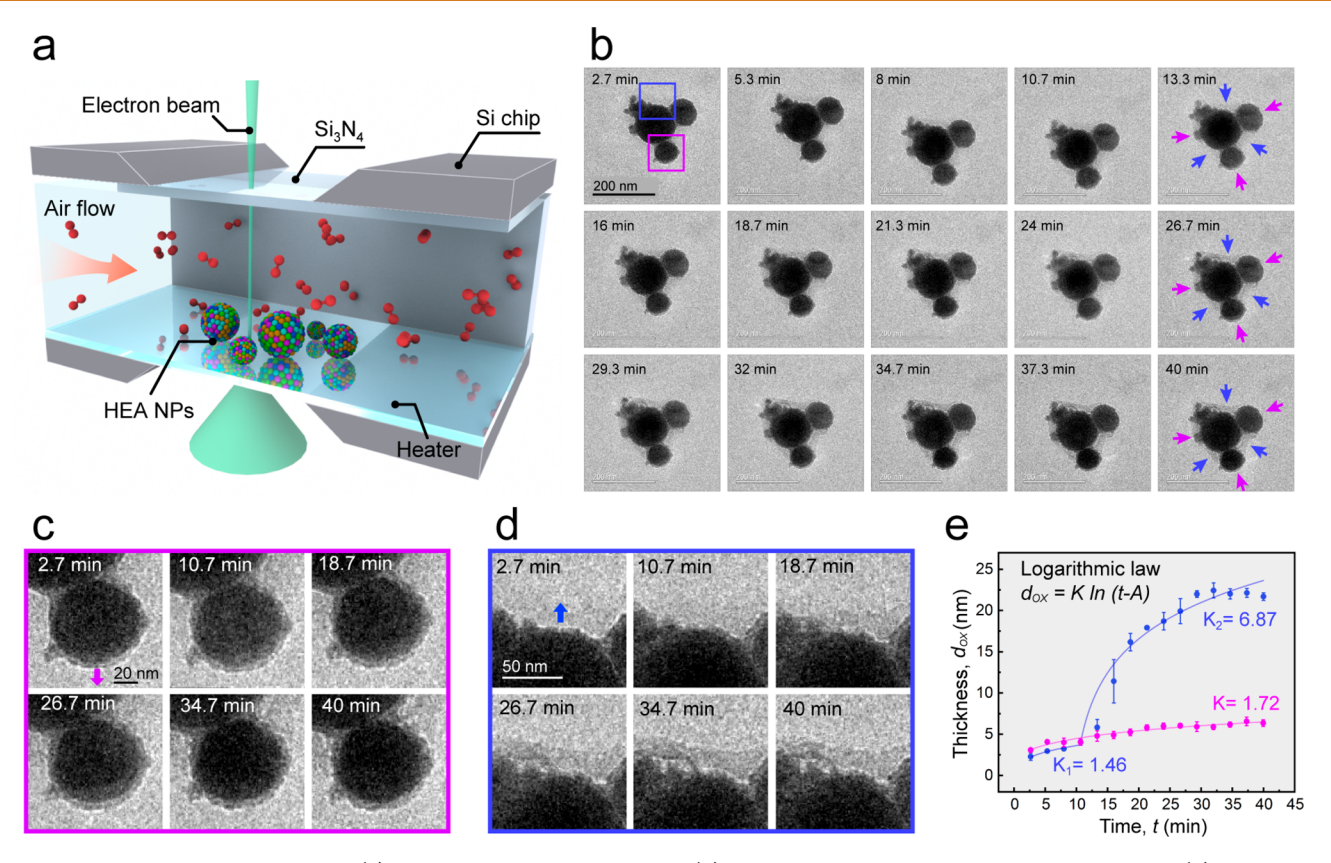


Figure 2. Oxidation of HEA NPs in air. (a) Schematic of the *in situ* gas-cell (S)TEM device to study the oxidation of HEA NPs. (b) *In situ* TEM image sequences of HEA NPs during annealing in air. (c, d) TEM image sequences focused on the two boxed regions in (b) during annealing in air. (e) Oxide thickness as a function of time measured from the direction highlighted in (c, d).

synthesized HEA NPs were characterized by STEM, EDS, and EELS. High-angle annular dark-field (HAADF) image in Figure 1a shows that the HEA NPs are mostly spherical with particle sizes ranging from 50 to 200 nm. Figure 1b is a low-angle annular dark-field (LAADF) image focused on an individual NP with faceted edges. The boxed region was selected for atomic resolution HAADF and annular bright-field (ABF) imaging, as shown in Figure 1c. The lattice distortion and random atom-toatom contrast variation suggests a homogeneous mixing of Fe, Co, Ni, Cu, and Pt at the atomic level. Inset in the ABF image shows the fast Fourier transform (FFT) patterns in the \langle 100 \rangle zone axis with $(00\overline{2})$ and (022) planes highlighted, confirming the successfully synthesized single-phase HEA NPs with facecentered cubic (fcc) crystal structure, which is consistent with our previous reported X-ray powder diffraction (XRD) results. 15 The composition uniformity was confirmed by both STEM-EELS and STEM-EDS mappings. STEM-EELS mapping was performed on a NP in (110) zone axis, as shown in Figure 1d. The crystal contains regions with appreciable twining, as suggested in FFT and marked by dashed lines. The EELS mappings in the red shadowed region from Fe, Co, Ni, Cu Ledges and Pt M-edge are shown in Figure 1e. In all cases, Fe, Co, Ni, Cu, and Pt are found to be distributed homogeneously. In addition, elemental distribution from STEM-EDS mapping in the sample region of Figure 1a is shown in Figure 1f. These further confirm that all the synthesized NPs, irrespective of their sizes, have well-mixed elemental compositions. The composition of each HEA NP is obtained from EDS analysis (Supporting Information Figure S1), and the averaged HEA composition is determined to be Fe_{0.28}Co_{0.21}Ni_{0.20}Cu_{0.08}Pt_{0.23}.

Figure 2a shows a schematic illustration of the specimen holder employed for the in situ gas-cell TEM experiments. Atmospheric pressure can be maintained inside the cell with continuous gas flow benefiting from the isolated environment formed by a pair of microchips. ^{29,34–36} The *in situ* experiment was performed in air environment as shown in Movie S1. The beginning of the movie is exactly at the same time as the start of the heating process. Snapshots from Movie S1 are shown in Figure 2b. The HEA NPs underwent oxidation in atmospheric air, and an oxide layer can be seen growing and gradually covering the NPs, shown as the lighter contrast layer on HEA NPs. To present this more visibly, the magnified images of the boxed regions in the first frame are shown in Figure 2c,d, with the purple box corresponding to one small NP (<100 nm) and the blue box focusing on the top surface of the larger NP ~ 130 nm. The small NP has a thin oxide layer all around the nanoparticle, while the oxide layer on large NP is thick and not uniform, which becomes noticeable starting from ~13.3 min. Compared to our in situ oxidation of monometallic Co NPs in similar size at 400 °C (Movie S2), it is clear that Co transferred from solid NPs to hollow structures in <1 min. Moreover, bimetallic alloy NPs were also observed to show full oxidation in < 30 min, forming porous and hollow structures such as NiFe NPs in air 23 and $\overline{\text{NiCr}}$ NPs in low pressure (1 mbar) $O_2^{\ 26}$ as well as the formation of obvious voids for NiCo NPs accompanied by the outward diffusion of Ni and Co.³⁷ For HEA NPs presented here, formation of voids and hollow structures in similar size ranges is not observed, suggesting that the overall oxidation kinetics are slower than both mono and bimetallic alloy NPs with similar principle elements. The oxide layer thickness d_{OX} is plotted in Figure 2e after measurement, following the same

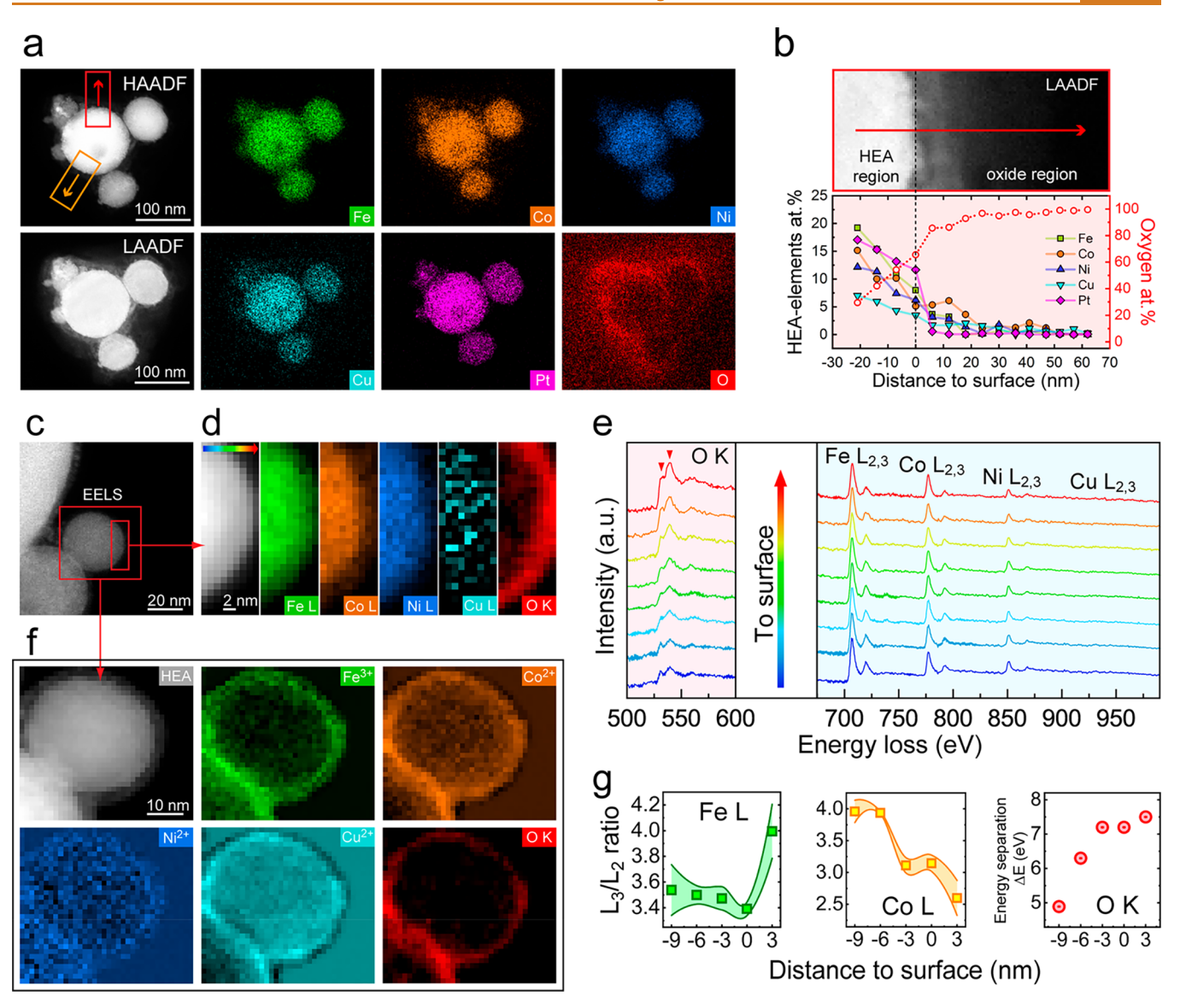


Figure 3. Chemical analysis of HEA NPs after oxidation in air. (a) Post situ HAADF and LAADF images of the same HEA NPs after in situ oxidation in Figure 2, followed by EDS mappings of Fe, Co, Ni, Cu, Pt, and O. (b) LAADF images from red boxed regions in (a) and corresponding at.% distribution of Fe, Co, Ni, Cu, Pt, and O extracted from EDS maps. The arrows in LAADF images indicate the same directions as the arrows in (a). The zero in the horizontal axis (distance to surface) represents the edge of NP marked by dash lines, while positive values stand for outward directions. (c) ADF image showing HEA NPs after ex situ oxidation in air. (d) Spectrum image corresponding to smaller red boxed region in (c) and EELS maps extracted from Fe, Co, Ni, Cu $L_{2,3}$ -edges and O K-edge. (e) EEL spectra extracted from the spectrum image in (d) in the direction marked by rainbow arrow. The O prepeak and main peak maximum marked with red arrows are highlighted with dash lines. (f) EELS MLLS fitting showing the valence state map from larger red boxed region in (c). The maps are displayed in sequence of fitting results from the reference spectra of as-synthesized HEA, Fe₂O₃, CoO, NiO, and CuO. The last map was extracted directly from the O K-edge. (g) Fe and Co L_3/L_2 white-line intensity ratio as a function of distance to surface obtained from another HEA NP after oxidation. Zero in the horizontal axis represents the edge of NP, while positive values stand for outward directions. The third plot shows the energy difference between O K-edge prepeak and main peak (energy separation, ΔE) as a function of distance to the HEA surface.

direction as indicated in the arrows in Figure 2c,d. For the small NP, oxidation kinetics can be perfectly fitted with a logarithmic law $d_{\rm OX} = K \ln(t-A)$, where the oxidation rate K is determined to be 1.72. The oxidation kinetics follow logarithmic law rather than parabolic as predicted by Wagner theory, ³⁸ suggesting that the growth of oxide layer is governed by combined effects involving the electric field and lattice diffusion. The reason could be that Wagner's theory assumes a planar geometry, while for HEA NPs considering the spherical geometry with surface curvature, the oxidation kinetics can be altered by surface charge and space charge distribution. Since there is much stronger polarization in spherical NP than planar surface, ³⁹ the electric

field⁴⁰ across the oxide in radial directions⁴¹ will result in a faster growth rate compared to the parabolic relationship in the initial stages and a slower rate in the longer time range that fits into the logarithmic law. As seen in Figure 2e, the larger NP, again follows logarithmic law with $K_1 = 1.46$ in the first 10.7 min but has a burst of oxide growth starting at ~13.3 min. The oxidation kinetics afterward can also be fitted with a logarithmic function with $K_2 = 6.87$, indicating a much faster oxidation rate. This anomalous two-stage oxidation kinetics seems to happen selectively at the region where two HEA NPs are adjacent (highlighted by blue arrows in Figure 2b), while the surface without adjacent NPs displays only one-stage oxidation kinetics

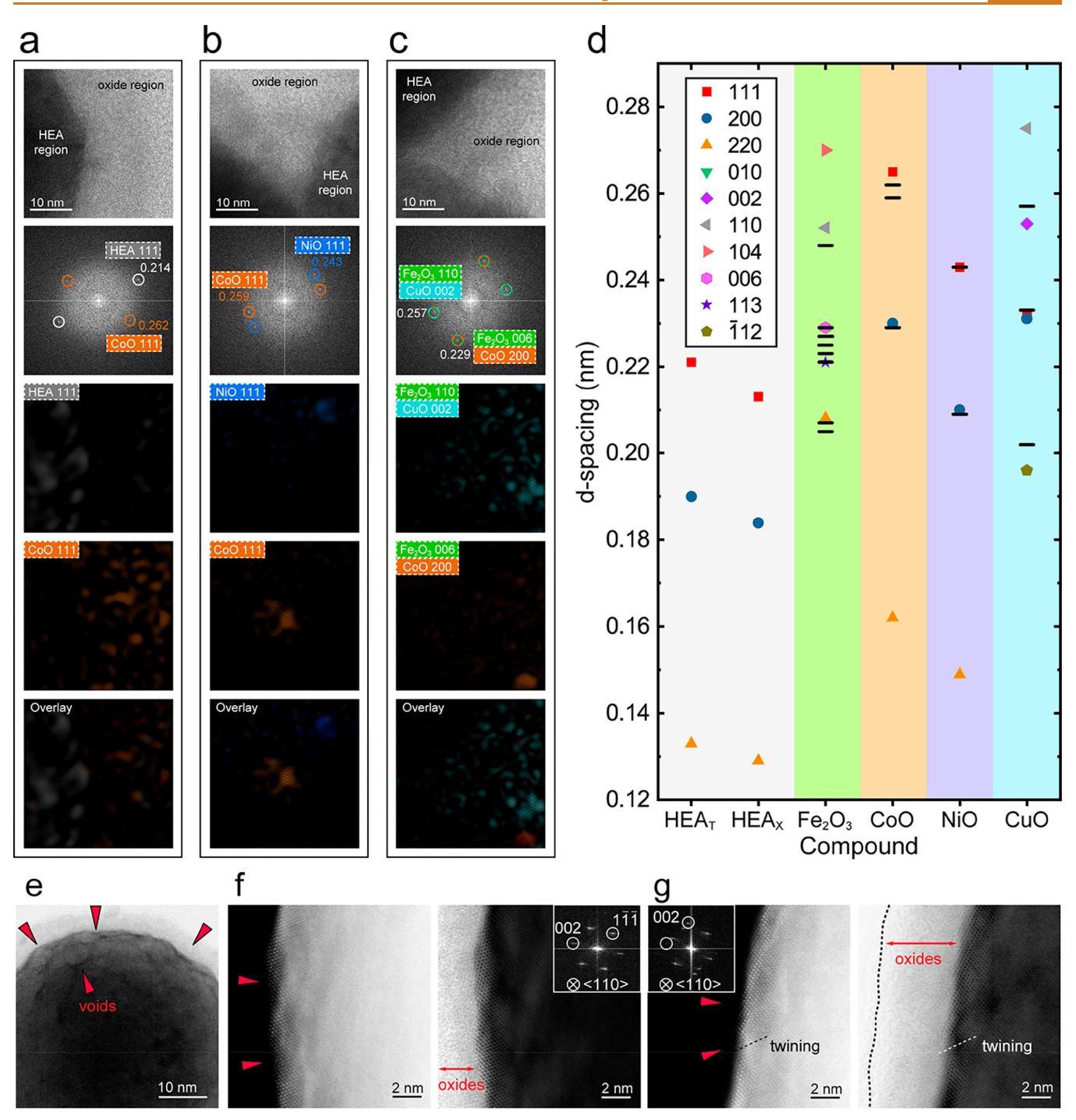


Figure 4. HRTEM analysis of HEA NPs after oxidation in air. (a–c) Three exemplar HRTEM images and the corresponding FFTs of HEA NPs after *in situ* oxidation in air. In the FFTs, diffraction spots are highlighted according to the most possible crystal planes in HEA or oxide phases. The last three rows show the IFFT of masked diffraction spots with corresponding phases and the overlaid image. (d) A portion of d-spacings in different crystal planes in as-synthesized HEA and various oxide compounds. Dash signs in oxide compounds mark the d-spacings obtained from HRTEM analysis. HEA_T stands for information extracted from (S)TEM analysis, and HEA_X are obtained from XRD results. For oxide compounds, only d-spacings larger than 0.195 nm are shown to avoid overlapping of data points. (e) ABF image of a HEA NP after ex situ oxidation showing plenty of voids <10 nm in length. (f) Atomic resolution HAADF and ABF images of a HEA NP edge after oxidation. Exemplar voids are marked by red arrows. The oxide layer is highlighted. Inset in the ABF image is the corresponding FFT showing the NP in $\langle 110 \rangle$ zone axis. (g) Atomic resolution HAADF and ABF images of a HEA NP in $\langle 110 \rangle$ zone axis. Exemplar voids are marked by red arrows, and the oxide layer is highlighted. A twining can be observed in both images marked with dash lines as well as in the FFT (inset in HAADF image) with two pairs of (002) diffraction spots.

(purple arrows in Figure 2b). Existing high-temperature oxidation models⁴² (Valensi–Carter and Fromhold) taking spherical geometry into consideration predict that smaller NPs can be oxidized faster than larger NPs, which is consistent with

our experimental observation within first ~ 10.7 min. The increased oxidation rate after 13.3 min for large NPs in the second oxidation stage may be attributed to the sintering induced atomic surface diffusive flux close to the interfaces

where HEA NPs are in contact,⁴³ resulting in a change of electric-field induced concentration gradient in initial oxide and provides extra driving force for metal outward diffusion.^{43–45} In addition, the oxidation kinetics of HEA NPs are compared with monometallic Co NPs, as plotted in Figure S2. The 55 nm Co NP oxide thickness increases to 25 nm in <1.2 min of oxidation, however there is no visible oxidation in HEA NPs at the same time frame. This confirms the much slower oxidation behavior in HEA NPs. The clear mechanisms are yet to be determined, while more systematic analysis on HEA NPs' properties is necessary, taking into account parameters such as built-in pressure, strain, ^{46,47} and electric field⁴¹ in such HEA NP systems.

To gain understanding on the chemical composition after oxidation, the HEA NPs were characterized by STEM-EDS and STEM-EELS as shown in Figure 3. HAADF and LAADF images in Figure 3a show the same HEA NP region after in situ oxidation. Apparently, the LAADF images show more clearly the oxide region with a brighter contrast due to the higher signal-tonoise ratio in scattering at low angles for oxygen-containing compounds. In the STEM-EDS maps, transition metals of Fe, Co, Ni, and Cu are all seen to present in the oxide layer, while Pt is the only metal that does not segregate to the surface. Combining with selected overlaid maps (Figure S3), it is clear that: (1) in the region without oxygen, HEA NPs still show a homogeneous mixing of Fe, Co, Ni, Cu, and Pt; (2) Fe, Co, Ni, and Cu can be found in the region with oxygen; and (3) Cu is the most widely dispersed in the oxide region. Further, quantitative EDS analysis was extracted from the maps in the two boxed regions, focusing on the large NP, and is shown in Figures 3b and S3b. The boxed regions were aligned with the plots with corresponding colors. The NP surface is defined as the boundary of the brightest contrast in LAADF images (marked by dashed lines) so the outward direction indicates the oxide region. The two plots show the same trends where Fe, Co, Ni and Cu show outward diffusion, while Pt does not display outward segregation and is not present in the oxide layer. Among the transition metals, Co is more accumulated in the oxide region closer to HEA surface within \sim 20 nm, Cu is more present in the region farther away, and Fe and Ni are distributed in a more monotonic decreasing manner in the oxide. These results show the oxidation of HEA NPs is guided by Kirkendall effects, where metals diffuse outward at different rates to react with oxygen. This leads to a composition variation in the oxide layer and HEA core. Further, to exclude the influence of electron beam during in situ observation, STEM-EDS on HEA NPs on other regions without the electron beam exposure is shown in Figure S4 and discussed in Supporting Note S1. The results show that there is no significant difference in composition and more Kirkendalls voids are seen in the larger HEA NPs.

The STEM-EELS analyses on ex situ oxidized HEA NPs are shown in Figure 3c–g (first method, details in the Methods section). The ADF image in Figure 3c shows the oxide layer on HEA NPs after oxidation, and the EELS mappings (Figure 3d) from the small red boxed region again confirm that the oxide layer contains Fe, Co, Ni, and Cu. The EEL spectra from the mapping region are then extracted following the direction of the rainbow arrow and are plotted in Figure 3e. Although subtle changes of transition-metal $L_{2,3}$ -edges are hard to discern in the current energy resolution, there are obvious variations on O K-edge, especially the prepeak intensity and energy separation between prepeak and main peak when it is closer to NP surface, as highlighted by red arrows. Further, with a larger EELS mapping area (larger boxed region in Figure 3c) covering the

whole HEA NP, multiple linear least-squares (MLLS) fitting results are shown in Figure 3f. The fitting is performed using Ledges reference spectra of as-synthesized HEA, Fe_2O_3 , CoO, NiO, and CuO $^{48-53}$ and is shown in the same sequence. The last image is a directly extracted O-K map for the ease of comparison. These MLLS fitting results serve as valence-state maps of Fe, Co, Ni, and Cu. It can be seen that Fe³⁺, Co²⁺, Ni²⁺, and Cu²⁺ are all present in the oxide layer region, suggesting that in the oxide, Fe is in a 3+ state, while Co, Ni, and Cu are in a 2+ state. This is consistent with a previous study⁵⁴ showing that among various stoichiometries of oxides, Fe₂O₃ and CuO are more favorable in high-oxygen concentrations. Figure 3g shows an energy loss near-edge fine structure (ELNES) of L_3/L_2 white-line intensity ratio for Fe and Co and O-K on another similar size HEA NP. It is known that the transition-metal L_3/L_2 white-line ratio is directly correlated with 3d orbital occupancy, where a higher ratio indicates an increased oxidation state for Fe,55 while a lower ratio indicates a higher oxidation state 56,57 for Co. Here, the Fe L_3/L_2 white-line ratio displays an increase in the external oxide (positive distance to surface) region, suggesting a more oxidized Fe state compared to the interior of HEA NP. Likewise, the Co L_3/L_2 white-line ratio gradually decreases from the NP interior to surface and drops further in the external oxide region, suggesting an upward gradient of the Co oxidation state. The third plot in Figure 3g shows the distance of O K-edge prepeak to the main peak (energy separation, ΔE) as a function of distance to HEA surface. Although the ELNES of O K-edge contains metal-oxygen bonding information contributed by four transition metals involving Fe, Co, Ni, and Cu, an increase of Δ E from interior to surface can still be identified, indicating the higher overall oxidation states in the oxide region.⁵⁸

Next, high-resolution TEM (HRTEM) images were successfully obtained on the HEA NPs discussed in Figure 2 after oxidation. The first row in Figure 4a-c shows exemplar HRTEM images with the HEA and oxide region highlighted. The corresponding FFTs are shown in the second row, with diffraction spots marked with d-spacings. Since the largest dspacing in fcc HEA NPs is 0.214 nm from {111} planes, any observed d-spacing larger than that should originate from the oxides. As such, in FFTs the diffraction spots are labeled as the most possible crystal planes from HEA or oxide compounds. Examples are shown as $\{111\}_{CoO}$ in Figure 4a, $\{111\}_{NiO}$ in Figure 4b, $\{110\}_{Fe_2O_3}$ or $\{002\}_{CuO}$, and $\{006\}_{Fe_2O_3}$ or $\{200\}_{CoO}$ in Figure 4c. To clearly validate the oxides, inverse FFTs (IFFTs) are shown in Figure 4a-c by masking each pair of diffraction spots. As seen, starting from the third row in Figure 4a, for instance, $\{111\}_{HEA}$ is only from HEA region, while $\{111\}_{CoO}$ is mostly in the oxide layer. Following the same trend, Figure 4b,c shows that crystal planes from oxide compounds are only present in oxidized regions. After carefully analyzing all the HRTEMs, the lattice *d*-spacings not likely to belong to HEA are plotted as dashed signs in Figure 4d. The *d*-spacings from planes in HEA and some oxide compounds are shown for reference. The first and second columns named HEA_T and HEA_X are based on (S)TEM and XRD analyses, respectively. Those d-spacings not belonging to HEA are likely to originate from oxides including Fe₂O₃, CoO, NiO, and CuO. The results show consistency with previous valence state analyses on ex situ oxidized HEA NPs where Fe3+, Co2+, Ni2+, and Cu2+ are identified. There are also possibilities that these ordered lattices originate from complex oxides involving more than one metal elements, however it is not possible to properly index them due

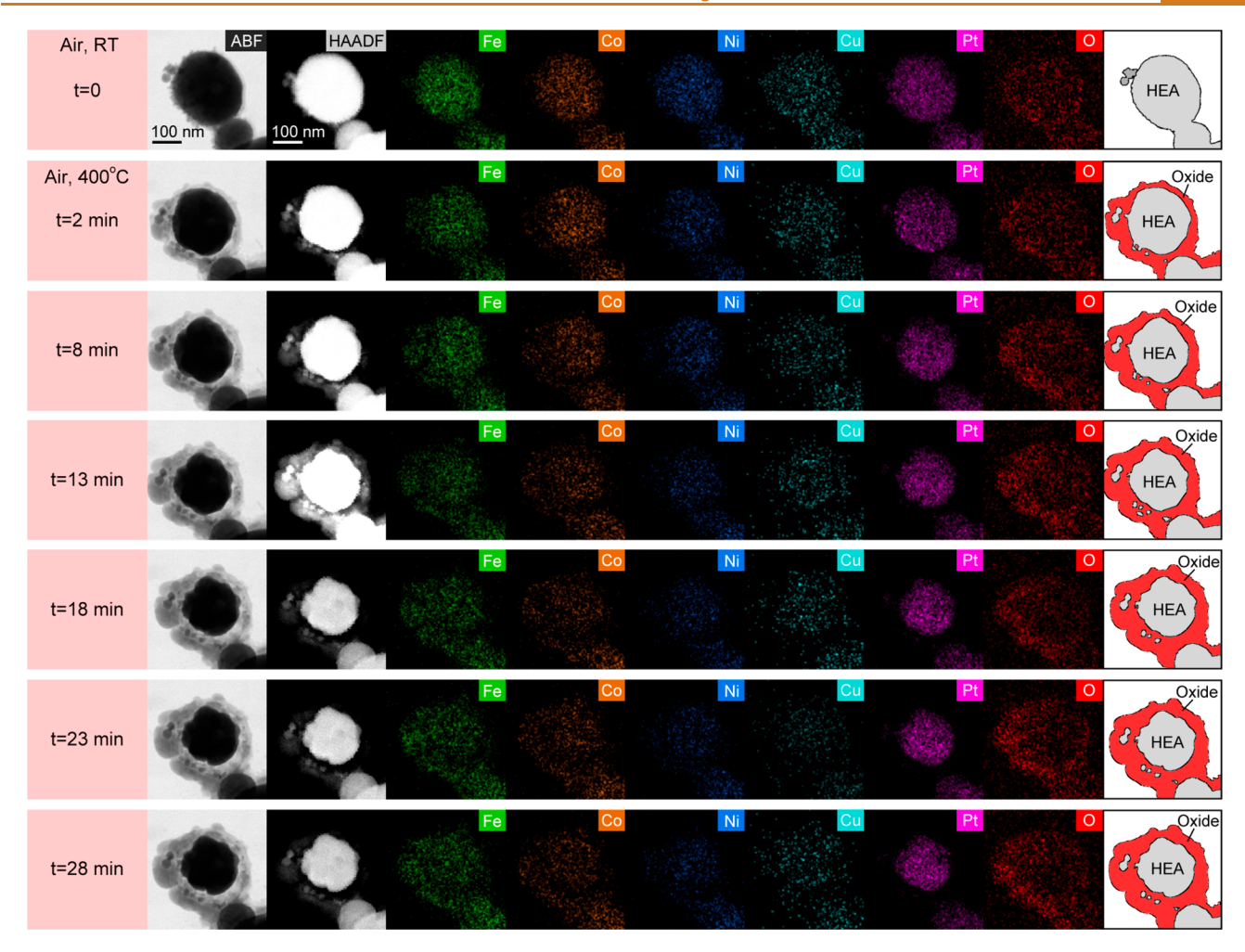


Figure 5. In situ EDS analysis of HEA NPs annealing in air at 400 °C. First column is time stamps. Second column is ABF images of HEA NPs annealing in air. Third column is HAADF images of the HEA NPs and corresponding EDS maps of Fe, Co, Ni, Cu, Pt, and O. Last column outlines the HEA NP and the oxide layer extracted from ABF images. The first row (t=0) corresponds to the condition at RT and is right before temperature ramping up to 400 °C.

to the lack of standard lattice parameters. The results further suggest that although the oxide lattices are not observed to be homogeneous in all oxide regions, there are ordered oxide crystallites in the disordered oxide matrix containing Fe, Co, Ni, Cu, and O. While principle elements including Fe, Co, Ni, and Cu typically form crystalline oxide under similar oxidation conditions, the observed disordered oxide with only localized oxide crystallites can be ascribed to sluggish diffusion and factors that lower the total Gibbs free energy of disordered oxide compared to crystalline oxide: (1) Atoms are expected to be trapped in their local positions if diffusion is sluggish and may form only short-range ordering that may not go beyond a few nanometers, (2) built-in high entropy in the HEA NPs that lower the positive contribution of interfacial energy between HEA and disordered oxide interface, ⁵⁹ and 3) the strain induced by the lattice mismatch between an epitaxial HEA and crystalline metal oxide interface at curvature regions that increase the interfacial energy contribution. 32 Therefore, compared to single element NPs, our atomistic studies show that HEA NPs can form disordered oxides. Considering disordered oxides can serve as a diffusion barrier 60 and the possible sluggish diffusion in HEA, they can be the reason that HEA NPs display slower oxidation kinetics compared to monometallic or bimetallic NPs.

The structural information is also studied on ex situ oxidized HEA NPs (first method in the Methods section). For the ABF image in Figure 4e, the oxide layer can be seen in the lower contrast region close to the HEA surface. A significant number of voids of <10 nm in size are clearly observed and exemplar of them marked by red arrows. Larger voids are expected to form after these tiny ones accumulate and coalesce. Figure 4f shows a pair of HAADF and ABF images of HEA NPs in the $\langle 110 \rangle$ zone axis. FFT (inset in ABF image) indicates an fcc pattern of HEA NPs. While no lattice can be resolved in the oxide layer region, clearly the HEA NP maintains its fcc structure as evident through the same atomic arrangement in comparison to the assynthesized sample (Figure 1d). This is true even at the void regions (marked by red arrows), suggesting that the atomic outward diffusion during oxidation does not break the fcc crystal structure. This is consistent with HRTEM in Figure 4a that {111}_{HEA} can be resolved. A pair of HAADF and ABF images in Figure 4g show another HEA NP in the (110) zone axis with identifiable twining (marked by dashed lines). Although it is not clear whether the twining existed initially or formed after oxidation, the fcc structure in HEA NP is confirmed to remain unchanged. This is also consistent with the second ex situ oxidation results (details in the Methods section) discussed in Supporting Note S2 and Figure S5.

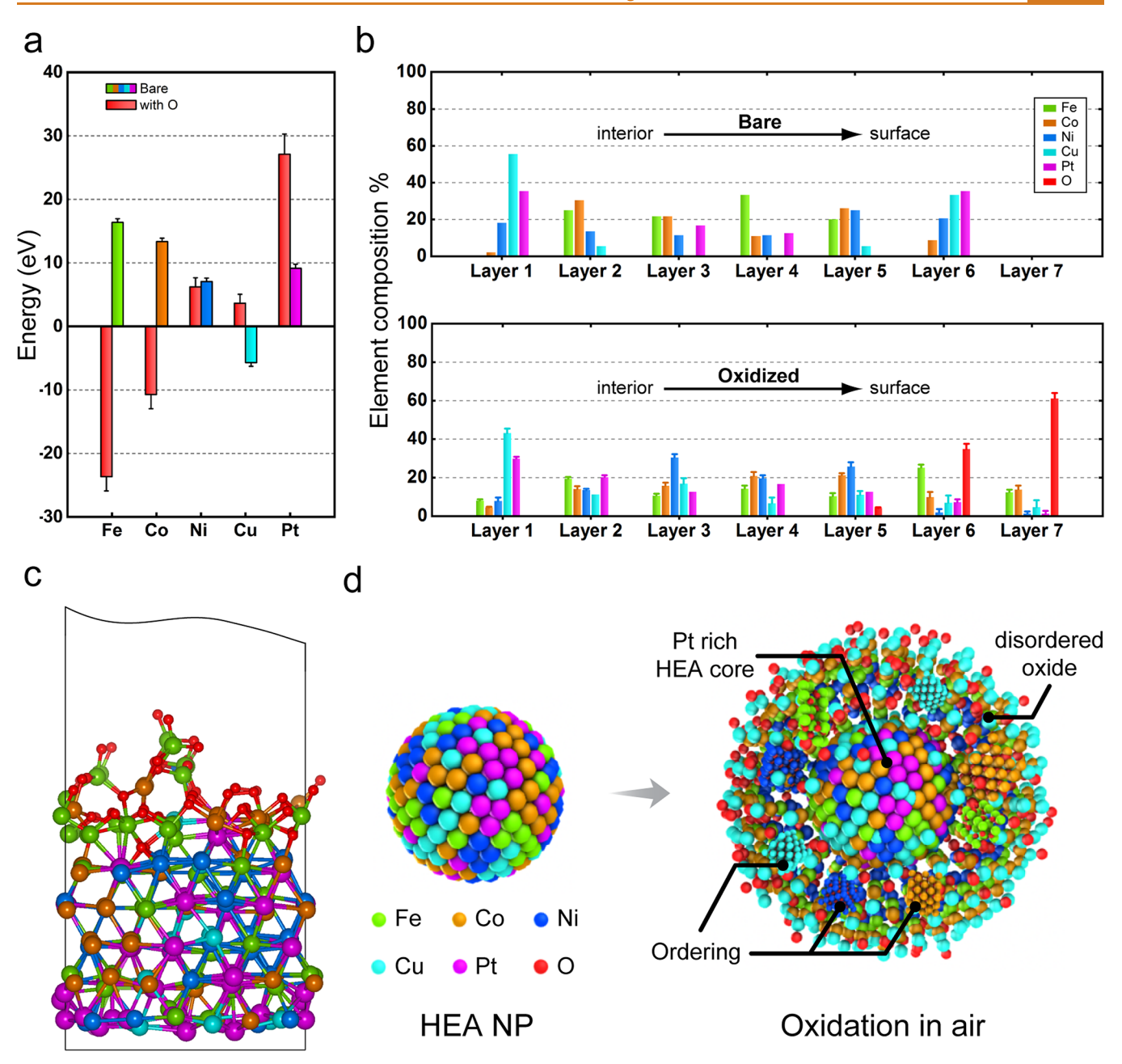


Figure 6. (a) Total energies for slab models with different elements segregation compared to the random alloy model. For each model, the corresponding energy of the oxidized surface is shown as red. Negative values indicate an enhanced stability compared to random alloy without accounting for configurational entropy. Statistical errors for the energies extracted from molecular trajectory are shown. (b) Equilibrium layer-by-layer surface composition for bare and oxidized surfaces at 400 °C. The error bars indicate statistical errors from equilibrium structures obtained from MC/MD. Oxidation increases the thickness of the slab and leads to the formation of an extra layer. (c) Exemplary atomic model for an oxidized slab from the MC/MD ensemble after equilibration. (d) Schematic illustration of the oxidation process of HEA NPs.

To further understand the compositional evolution in real time, *in situ* STEM-EDS are performed and shown in Movie S3. The HEA NP in the upper left corner is magnified and shown in Figure 5. The ABF and HAADF images are displayed together with EDS maps for Fe, Co, Ni, Cu, and O at different times. Outlines of HEA and the oxide layer are also shown in the last column. At room temperature (RT), the HEA NPs show homogeneous mixing of all five elements with 2–3 nm native oxide covering the surface. The oxide contains Fe, Co, Ni, and Cu and is expected to originate from the initial stage of oxidation driven by the Mott electric field in the oxide layer, as predicted by the Cabrera–Mott model.⁶¹ At 400 °C, the oxide layer begins

to grow, and after 2 min it is denser on left side where two adjacent NPs are present. The gradual outward diffusion of Fe, Co, Ni and Cu evidenced through EDS maps again confirms that the oxidation is guided by the Kirkendall effect. This outward diffusion of transition metals and vacancies results in the formation of voids close to HEA surface. Then voids coalesce, leading to the shrinkage of HEA NPs and notable segregation of Fe, Co, Ni, and Cu to the outer oxide. In addition, the *in situ* STEM-EDS analyses suggest that the outward diffusion of transition metals occurs almost simultaneously from the beginning at 400 °C due to atomic homogeneity of assynthesized HEA. Thus, the composition gradient in the formed

oxide is mainly induced by different diffusion rates among transition metals. Figure S6 shows the Arrhenius plots of diffusion coefficients for Fe, Co, Ni, and Cu in their oxides, and Table S1 lists the values at 400 °C in relationship to atomic radius. Fe has the highest diffusibility at 400 °C followed by Cu, Co, and Ni, which is in partial agreement with experimental observations that outward diffusion of Fe and Cu is more notable than Co and Ni. However, the diffusion coefficient does not follow the decreasing trend of atomic radius from Fe to Cu (Fe > Co > Ni > Cu) and cannot explain why Cu shows the farthest diffusion distance from the HEA surface, while a possible explanation may be due to the highest vapor pressure of Cu among all investigated metals. 15 Future investigations of metal diffusibility and activation energy for each element in other possible oxide matrices with more than one metal element are necessary to obtain a systematic understanding.

To confirm that the phase segregation is only induced by air, in situ annealing of HEA NPs in vacuum environment is discussed in Supporting Note S3 and Figure S7. In addition, the electron dose rate during the *in situ* oxidation is approximately $40 \text{ e}^-/\text{Å}^2/\text{s}$, which is 2 orders of magnitude lower than the threshold dose rate for electron damage on oxides ⁶² and also lower than other electron-beam-induced oxidation studies. The results further suggest the observed phase segregation is induced by oxidizing environments instead of electron beam effects.

Next, density functional theory (DFT) calculations were carried out to further understand the oxidation process of the HEA NPs. First, the stability of a bulk random alloy consistent with the $\mathrm{Fe_{0.28}Co_{0.21}Ni_{0.20}Cu_{0.08}Pt_{0.23}}$ chemical composition that is inferred experimentally was investigated. The energies of several random models of the alloy assuming a HEA phase with fcc or body-centered cubic (bcc) lattice symmetry were compared. After a full structural optimization, it is found that the fcc system is 0.05 eV/atom lower in energy than the bcc one. Thus, the alloy has an fcc symmetry that agrees with the experimental results. In addition, the optimum lattice constant of the fcc lattice is found to be 3.61 Å, which correlates to a *d*-spacing of 2.1 Å for {111} planes and is very close to the experimentally determined *d*-spacing of 2.2 Å for the same planes.

The aforementioned DFT simulations employed few structural models for the alloy and thus cannot describe the configurational entropy that is key for the stability of HEAs. To address this shortcoming, calculations using a hybrid MC/MD approach based on energies and forces computed with DFT were carried out. This scheme employs short ab initio MD runs and random exchange between atoms at different locations, in which the last configuration is accepted or rejected using a standard Metropolis algorithm. 64,65 There are several advantages for the employed MC/MD approach as it automatically accounts for temperature, mixing entropy, and atomic vibrations, while describing all interactions in the systems within first-principles methods. Following the MC/MD simulations, it is found that in equilibrium, the alloy has a uniform distribution of the elements. Also, consistent with the static full optimization calculations, the HEA with fcc symmetry is found to be ~ 0.05 eV/atom lower in energy than that of the bcc one at all investigated temperatures 100-900 °C (Figure S8).

Further, the impact of oxidation on the stability of the HEAs was studied. First, the stabilization energies due to potential segregation under oxidizing conditions were examined. Five

alloy models that differ in the identity of the element enriching the top layer but is random otherwise were constructed in addition to three different alloy models with a complete random distribution. In these studies, surface slab models well representing the large ~50-200 nm NPs that are seen experimentally were employed. Further, a smaller ~1 nm NP (Figures S9-S11) was verified to display similar energy preferences. The oxidizing conditions are modeled by adsorbing oxygen on the top surface. 66-69 Starting from the initial configuration constructed using fcc with a lattice constant of 3.61 Å, the atomic positions were relaxed to a ground-state equilibrium structure at T = 0 K, and then a 4 ps *ab initio* MD trajectory within NVT ensemble (constant number of particles, volume, and temperature) at T = 400 °C was conducted. Figure 6a shows the energies of the different models averaged over the last 2 ps measured with respect to the random alloy model. As seen, Fe, Co, and Pt segregated surfaces have high energies due to their large surface energies compared to that of Ni and Cu.⁷⁰ It is noted that the high entropy of mixing is not included in the energies of Figure 6a. Hence segregated models that have lower energies than the random alloy one such as the Cu-rich surface are not indicative that segregation is preferable for the pristine surface. For instance, based on ideal mixing of the elements, the configuration entropy $-k_{\rm B}\sum_{i=0}^{5}x_{i}\ln x_{i}$ (where $k_{\rm B}$ is Boltzmann constant and x_i is the metal concentration) lowers the free energies by ~0.09 eV/atom for the alloy at 400 °C. As will be shown later, there is no element segregation for the pristine HEA surfaces when configurational entropy is accounted for by employing the hybrid MC/MD approach.

As seen from the energies in Figure 6a, oxidation significantly stabilizes surfaces that are rich in Fe and Co compared to the random alloy, and to a lesser extent surfaces rich in Ni and Cu. However, Pt-rich surfaces have a significantly higher energy compared to the random alloy surface. Thus, under oxidation, surfaces of the NPs are expected to be poor in the noble metal Pt but rich in Fe and Co, and to a lesser extent Cu and Ni. The obtained energy trends for the oxidized slab models can be rationalized by examining the formation energies of the corresponding bulk oxides. For the metal oxides, the order of the formation energies is Fe (1.7), Co (1.3), Cu (1.0), Ni (0.9), and Pt (0.6) with the numbers in parentheses showing the DFT formation energies in eV/atom. Thus, Fe forms the most stable oxide with a formation energy of 1.7 eV/atom, and Pt is the least stable one with 0.6 eV/atom. Similar conclusions can also be reached by inspecting the Ellingham diagrams of these oxides.

MC/MD simulations are then carried out for the slab models to determine their equilibrium composition while accounting for temperature and entropy effects. Figure 6b shows a layer-bylayer surface decomposition obtained by analyzing equilibrium configurations from the MC/MD simulations. An exemplary configuration is shown in Figure 6c. As seen from the figure, there is a strong segregation preference for some elements to the top layers under oxidation conditions. For instance, compared to the bare surface, there is a notable enrichment of Fe and Co in the top exposed layers, but a significant reduction of Pt. This is also consistent with the trends inferred from the energies of the segregated models of Figure 6a. Further, the oxidation process increases the thickness of the substrate, resulting in the formation of an additional layer. As seen in Figure 6c, an equilibrium configuration during the oxidation shows the formation of vacancies in subsurface layers due to a Kirkendall effect from the inequivalent inner/outer diffusion of oxygen/ metal. Also, the oxidized slab models retain fcc symmetry away from the surface, again consistent with the experimentally observed fcc lattices after oxidation. Although the slab models are relatively small to show the formation of any nanocrystalline oxides, Bader charge analysis in Table S2 suggests that the chemical environment of the metals in the oxide layer is similar to the corresponding Fe_2O_3 , CoO, NiO, and CuO oxides that are inferred experimentally.

The schematic shown in Figure 6d illustrates the oxidation process of HEA NPs. The HEA NPs are initially homogeneously mixed in the atomic level at RT, while at 400 °C in air, the outward diffusion of transition metals resulted in the oxide layer enriched with Fe, Co, Ni, and Cu. Kirkendall effects guided the process and lead to a concentration gradient in the oxide. Localized ordered lattices from transition-metal oxides can be seen to form in the overall disordered oxide region. The HEA core retains a fcc structure but shrinks in size due to deficiency of transition metals. Nonreactive Pt stays in the HEA core region at all times during the oxidation process. The formed disordered oxide serves as diffusion barrier to prevent further oxidation of the HEA core, resulting in a logarithmic rate constant for oxidation kinetic that differs from the conventional high-temperature oxidation theory.

CONCLUSION

The present work reports in situ TEM observations and DFT studies of phase segregation in HEA NPs during hightemperature oxidation processes. The oxidation of HEA NPs is governed by Kirkendall effects with logarithmic rate constants that differ from high-temperature oxidation theory with parabolic prediction and is much slower than the oxidation of monometallic and bimetallic NPs. HRTEM and analytical EDS/ EELS provide direct evidence of transition metals segregation by outward diffusion and disordered oxide layer formation. The possible sluggish diffusion in HEA and formation of disordered oxide can slow down the oxidation kinetics compared to conventional monometallic and bimetallic systems. In addition, localized ordering is identified in the oxide layer that can originate from Fe₂O₃, CoO, NiO, and CuO crystallites. Simulations using hybrid MC/MD simulations based on DFT energies and forces confirm the stabilization of the alloy solution for the bare and oxidized surfaces and show that the oxidation drives Fe, Co, Ni, and Cu segregation to the top layers in agreement with experimental results. The present study is crucial for understanding HEA behavior in oxidizing environments and provides insights in designing high-temperature-resistant materials, durable catalysts, and corrosion-resistance alloys for various applications.

METHODS

HEA NPs Synthesis. HEA NPs containing Fe, Co, Ni, Cu, and Pt were synthesized based on the method in a previous study ¹⁵ and stored in a glovebox under Ar. The as-synthesized samples were dispersed in ethanol and sonicated for 2 min in a bath sonicator (Branson 3800, 40 kHz, 110W) before (S)TEM experiments.

In Situ TEM Experiment in Vacuum. A furnace-based heating holder (Gatan, Inc.) is used for heating experiments in vacuum conditions. HEA sample dispersion is drop-casted onto a Mo grid and then inserted into a spherical aberration-corrected JEOL JEM-ARM 200CF with a cold field emission source operating at 200 kV. Temperature was ramped up from RT to 400 °C with a 100 °C interval every 1 h and ramped down to RT after another 1 h staying at 400 °C.

In Situ Gas Flow TEM Experiment. A Hummingbird Scientific gas-cell TEM holder was used (Figure 2a). One μ L of HEA sample dispersion was drop-casted on a microchip equipped with a heater and

dried under air, then paired with another microchip to assemble the holder. The microchips have an electron transparent silicon nitride (Si₃N₄) viewing window with 50 nm in thickness. The distance between top and bottom microchip was controlled by a 250 nm spacer. All gases are flowed under constant volumetric flow rate of 0.5 sccm with the pressure inside the cell at approximately 1 atm. After loading the holder and flowing 100% pure nitrogen (N₂) gas at RT for 30 min, the gas was changed to dry laboratory grade air (containing ~21 vol % O₂), and temperature was ramped up to 400 °C within 2 min and kept constant afterward. When finished, the temperature was ramped down back to RT within 1 min. Unless otherwise specified, the electron beam was kept blocked all time except during the initial TEM alignment, focusing, and image acquisition to minimize electron beam effects. All *in situ* TEM experiments were carried out using a field emission JEOL 2100F microscope operated at 200 kV.

In Situ Gas Flow STEM Experiment. The *in situ* STEM and EDS experiments were performed using spherical aberration-corrected JEOL JEM-ARM 200CF with a cold field emission source operating at 200 kV combined with a gas-cell TEM holder from Protochips, Inc. The spacer distance between two microchips was 5 μ m. The holder was assembled after the HEA samples were drop-casted onto one of the microchips. Gas channels were opened to allow the sample exposure to air for the oxidation process. The local temperature was monitored in real-time and kept constant at 400 °C. In situ EDS maps were acquired with JEOL dual silicon drift detectors. The area of a single detector was 100 mm², and the solid angle for this dual EDS system was 1.8 sr. EDS maps were collected at RT and every 5 min at 400 °C.

Ex Situ Annealing Experiment in Air. Ex situ oxidation was performed in two different methods. In the first method, HEA NPs were first drop-casted onto Mo grid. The grid was placed onto a hot plate in an air atmosphere with the temperature preset to 400 °C for 1 h. Then the grid was cooled down in air before (S)TEM characterization. In the second method, the gas-cell TEM holder was assembled with HEA NPs but was not inserted into the microscope. The holder was then flowed with air, and temperature ramped up in same way as the *in situ* TEM experiment. After finishing and cool down to RT, the HEA NPs on microchip are characterized directly by (S)TEM.

Electron Microscopy Characterization. Post situ samples on microchips were characterized using a self-designed (S)TEM specimen holder (patent pending). STEM images were acquired by a spherical aberration-corrected JEOL JEM-ARM 200CF with a cold field emission source operating at 200 kV, at 22 mrad convergence semi-angle. Post situ EDS maps were acquired with Oxford X-Max 100TLE windowless silicon drift detector. EELS were acquired using a Gatan GIF Quantum spectrometer with an entrance aperture of 5 mm in dual-EELS mode. EELS maps were extracted from transition metals $L_{2,3}$ -edges, O K-edge using power law fitting background subtraction after energy drift correction, and Fourier-ratio deconvolution. The transition-metal L_3/L_2 white-line intensity ratio was determined by applying Hartree—Slater cross section step functions following the previous reported method. S6

Density Functional Theory Calculations. First-principles DFT calculations are employed using the Perdew-Burke-Ernzerhof exchange-correlation functional to solve the Kohn-Sham equations. The electronic self-consistent loops are terminated with an energychange tolerance of 1×10^{-8} eV. Bulk calculations for the alloy or for the elementary metals, or their oxides and hydrides, are carried out using the Vienna ab initio simulation package (VASP)72-74 with a planewave cutoff of 400 eV. For these calculations, we used a dense Γ centered k-grid with a 0.24 Å^{-1} spacing between k-points. This is equivalent to an $8 \times 8 \times 8$ mesh for bulk metals with a conventional four atom fcc unit cell. The electron-nucleus interactions are described using the projector augmented wave (PAW) method as implemented in VASP. 75 The hybrid MC/MD simulations are carried out using VASP computed energies and forces. For these calculations, we employed softer PAW potentials, a 300 eV planewave cutoff, and Γ point sampling of the Brillouin zone. It is found that equilibrium is reached by conducting a total of 1000 steps where each hybrid step corresponds to a potential MC swap between two random metal atoms followed by 40 molecular dynamics steps with a 1 fs time step. 65 The ab initio MD simulations for the slab models or the isolated NPs are carried out using CP2K with the DZVP-MOLOPT-SR-GTH basis sets and GTH norm-conserving potentials. 76,77 All of the calculations are done within the spin-averaged approximation. For the bulk fcc random alloy model, spin-polarized calculations yield a lattice constant 3.67 Å, which is close to the value of 3.61 Å obtained from spin-unpolarized calculations.

ASSOCIATED CONTENT

Supporting Information

The Supporting Information is available free of charge at https://pubs.acs.org/doi/10.1021/acsnano.0c05250.

As-synthesized HEA NPs composition (Figure S1); comparison between HEA NPs and monometallic Co NPs oxidation kinetics (Figure S2); post situ STEM-EDS results of HEA NPs in Figure 3a (Figure S3); STEM-EDS on HEA NPs without electron beam exposure (Supporting Note S1 and Figure S4); structural characterization of HEA NPs before and after ex situ oxidation (Supporting Note S2 and Figure S5); Arrhenius plots of diffusion coefficient with temperature (Figure S6); diffusion coefficient from Figure S6 and atomic radius (Table S1); in situ annealing of HEA NPs in vacuum (Supporting Note S3 and Figure S7); comparison between fcc and bcc energies of HEA from simulations (Figure S8); models for HEA NPs before (Figure S9) and after oxidation (Figure S10); normalized energies for the models in Figure S9 and S10 in comparison with random alloy model (Figure S11); Bader charge analysis for several metals and oxides (Table S2) (PDF)

Movie S1: *In situ* TEM video of HEA NPs oxidation in air at 400 °C 64 times faster (MP4)

Movie S2: *In situ* TEM video showing Co NPs oxidation in air at 400 °C 4 times faster (MP4)

Movie S3: *In situ* STEM-EDS maps of HEA NPs oxidation in air at 400 °C (MP4)

AUTHOR INFORMATION

Corresponding Authors

Reza Shahbazian-Yassar — Department of Mechanical and Industrial Engineering, University of Illinois at Chicago, Chicago, Illinois 60607, United States; ○ orcid.org/0000-0002-7744-4780; Email: rsyassar@uic.edu

Yuzi Liu — Center for Nanoscale Materials, Argonne National Laboratory, Argonne, Illinois 60439, United States;

orcid.org/0000-0002-8733-1683; Email: yuziliu@anl.gov Wissam A. Saidi — Department of Mechanical Engineering and

Materials Science and Pittsburgh Quantum Institute, University of Pittsburgh, Pittsburgh, Pennsylvania 15261, United States;
orcid.org/0000-0001-6714-4832; Email: alsaidi@pitt.edu

Michael R. Zachariah — Department of Chemical Engineering and Materials Science, University of California Riverside, Riverside, California 92521, United States; occid.org/0000-0002-4115-3324; Email: mrz@engr.ucr.edu

Authors

Boao Song — Department of Mechanical and Industrial Engineering, University of Illinois at Chicago, Chicago, Illinois 60607, United States; orcid.org/0000-0003-3124-3235

Yong Yang — Department of Chemical and Biomolecular Engineering, University of Maryland, College Park, Maryland 20742, United States; Department of Chemical Engineering and Materials Science, University of California Riverside, Riverside, California 92521, United States; orcid.org/0000-0001-5169-1479 Muztoba Rabbani — Department of Mechanical Engineering and Materials Science, University of Pittsburgh, Pittsburgh, Pennsylvania 15261, United States

Timothy T. Yang — Department of Mechanical Engineering and Materials Science and Pittsburgh Quantum Institute, University of Pittsburgh, Pittsburgh, Pennsylvania 15261, United States;
orcid.org/0000-0002-5785-0511

Kun He — Department of Materials Science and Engineering, International Institute for Nanotechnology (IIN), Northwestern University Atomic and Nanoscale Characterization Experimental (NUANCE) Center, Northwestern University, Evanston, Illinois 60208. United States

Xiaobing Hu − Department of Materials Science and Engineering, International Institute for Nanotechnology (IIN), Northwestern University Atomic and Nanoscale Characterization Experimental (NUANCE) Center, Northwestern University, Evanston, Illinois 60208, United States; orcid.org/0000-0002-9233-8118

Yifei Yuan — Department of Mechanical and Industrial Engineering, University of Illinois at Chicago, Chicago, Illinois 60607, United States; orcid.org/0000-0002-2360-8794

Pankaj Ghildiyal – Department of Chemical Engineering and Materials Science, University of California Riverside, Riverside, California 92521, United States

Vinayak P. Dravid — Department of Materials Science and Engineering, International Institute for Nanotechnology (IIN), Northwestern University Atomic and Nanoscale Characterization Experimental (NUANCE) Center, Northwestern University, Evanston, Illinois 60208, United States; orcid.org/0000-0002-6007-3063

Complete contact information is available at: https://pubs.acs.org/10.1021/acsnano.0c05250

Author Contributions

B.S. and R.S.-Y. conceived the idea. Y.Y., P.G., and M.Z. prepared the HEA samples. B.S. carried out the (S)TEM and *in situ* TEM experiments. M.R., T.Y., and W.S. carried out the DFT calculations. Y.L., K.H., X.H., Y.Y., and V.D. provided necessary (S)TEM support. B.S. wrote the paper under the direction of R.S.-Y. All authors contributed to the discussion and writing of the manuscript.

Notes

The authors declare no competing financial interest.

ACKNOWLEDGMENTS

R.S.-Y. acknowledges financial support from the National Science Foundation (award no. DMR-1809439). W.S. acknowledges financial support from the National Science Foundation (award no. DMR-1809085). T.Y. acknowledges a graduate student award from the Pittsburgh Quantum Institute. The computational work is supported in part by the University of Pittsburgh Center for Research Computing through the resources provided and the Argonne Leadership Computing Facility, which is a DOE Office of Science User Facility supported under contract DE-AC02-06CH11357. This work was performed, in part, at the Center for Nanoscale Materials, a U.S. Department of Energy Office of Science User Facility, and supported by the U.S. Department of Energy, Office of Science, under contract no. DE-AC02-06CH11357. This work made use of the JEOL JEM-ARM 200CF and JEOL JEM-3010 in the Electron Microscopy Service (Research Resources Center, UIC). The acquisition of the UIC JEOL JEM-ARM 200CF was supported by a MRI-R2 grant from the National Science

Foundation (DMR-0959470). We thank Dr. Fengyuan Shi from UIC for the assistance on (S)TEM experiments. Some of this work made use of the EPIC facility of Northwestern University's NUANCE Center, which has received support from the Soft and Hybrid Nanotechnology Experimental (SHyNE) Resource (NSF ECCS-1542205), the MRSEC program (NSF DMR-1720139) at the Materials Research Center, the International Institute for Nanotechnology (IIN), the Keck Foundation, and the State of Illinois, through the IIN. M.Z. acknowledges support from an ONR MURI.

REFERENCES

- (1) Tsai, M.-H.; Yeh, J.-W. High-Entropy Alloys: A Critical Review. *Mater. Res. Lett.* **2014**, *2*, 107–123.
- (2) Ye, Y. F.; Wang, Q.; Lu, J.; Liu, C. T.; Yang, Y. High-Entropy Alloy: Challenges and Prospects. *Mater. Today* **2016**, *19*, 349–362.
- (3) Chen, J.; Zhou, X.; Wang, W.; Liu, B.; Lv, Y.; Yang, W.; Xu, D.; Liu, Y. A Review on Fundamental of High Entropy Alloys with Promising High—Temperature Properties. *J. Alloys Compd.* **2018**, 760, 15–30.
- (4) George, E. P.; Raabe, D.; Ritchie, R. O. High-Entropy Alloys. *Nature Reviews Materials* **2019**, *4*, 515–534.
- (5) Yeh, J. W.; Chen, S. K.; Lin, S. J.; Gan, J. Y.; Chin, T. S.; Shun, T. T.; Tsau, C. H.; Chang, S. Y. Nanostructured High-Entropy Alloys with Multiple Principal Elements: Novel Alloy Design Concepts and Outcomes. *Adv. Eng. Mater.* **2004**, *6*, 299–303.
- (6) Otto, F.; Yang, Y.; Bei, H.; George, E. P. Relative Effects of Enthalpy and Entropy on the Phase Stability of Equiatomic High-Entropy Alloys. *Acta Mater.* **2013**, *61*, 2628–2638.
- (7) Fu, Z.; Chen, W.; Wen, H.; Zhang, D.; Chen, Z.; Zheng, B.; Zhou, Y.; Lavernia, E. J. Microstructure and Strengthening Mechanisms in an Fcc Structured Single-Phase Nanocrystalline Co₂₅Ni₂₅Fe₂₅Al_{7.5}Cu_{17.5} High-Entropy Alloy. *Acta Mater.* **2016**, *107*, 59–71.
- (8) Sriharitha, R.; Murty, B. S.; Kottada, R. S. Alloying, Thermal Stability and Strengthening in Spark Plasma Sintered Alxcocrcufeni High Entropy Alloys. *J. Alloys Compd.* **2014**, *583*, 419–426.
- (9) Fang, S.; Chen, W.; Fu, Z. Microstructure and Mechanical Properties of Twinned Al_{0.5}CrFeNiCo_{0.3}C_{0.2} High Entropy Alloy Processed by Mechanical Alloying and Spark Plasma Sintering. *Mater. Eng. (Reigate, U. K.)* **2014**, *54*, 973–979.
- (10) Zou, Y.; Wheeler, J. M.; Ma, H.; Okle, P.; Spolenak, R. Nanocrystalline High-Entropy Alloys: A New Paradigm in High-Temperature Strength and Stability. *Nano Lett.* **2017**, *17*, 1569–1574. (11) Brif, Y.; Thomas, M.; Todd, I. The Use of High-Entropy Alloys in Additive Manufacturing. *Scr. Mater.* **2015**, *99*, 93–96.
- (12) Fujieda, T.; Shiratori, H.; Kuwabara, K.; Kato, T.; Yamanaka, K.; Koizumi, Y.; Chiba, A. First Demonstration of Promising Selective Electron Beam Melting Method for Utilizing High-Entropy Alloys as Engineering Materials. *Mater. Lett.* **2015**, *159*, 12–15.
- (13) Gorsse, S.; Hutchinson, C.; Gouné, M.; Banerjee, R. Additive Manufacturing of Metals: A Brief Review of the Characteristic Microstructures and Properties of Steels, Ti-6Al-4V and High-Entropy Alloys. Sci. Technol. Adv. Mater. 2017, 18, 584–610.
- (14) Yao, Y.; Huang, Z.; Xie, P.; Lacey, S. D.; Jacob, R. J.; Xie, H.; Chen, F.; Nie, A.; Pu, T.; Rehwoldt, M.; Yu, D.; Zachariah, M. R.; Wang, C.; Shahbazian-Yassar, R.; Li, J.; Hu, L. Carbothermal Shock Synthesis of High-Entropy-Alloy Nanoparticles. *Science* **2018**, 359, 1489–1494.
- (15) Yang, Y.; Song, B.; Ke, X.; Xu, F.; Bozhilov, K. N.; Hu, L.; Shahbazian-Yassar, R.; Zachariah, M. R. Aerosol Synthesis of High Entropy Alloy Nanoparticles. *Langmuir* **2020**, *36*, 1985–1992.
- (16) Shi, Y.; Yang, B.; Liaw, P. Corrosion-Resistant High-Entropy Alloys: A Review. *Metals* **2017**, *7*, 43.
- (17) Daoud, H. M.; Manzoni, A. M.; Völkl, R.; Wanderka, N.; Glatzel, U. Oxidation Behavior of $Al_8\,Co_{17}\,Cr_{17}\,Cu_8\,Fe_{17}\,Ni_{33}$, $Al_{23}Co_{15}Cr_{23}Cu_8Fe_{15}Ni_{15}$, and $Al_{17}Co_{17}Cr_{17}Cu_{17}Fe_{17}Ni_{17}$ Compositionally Complex Alloys (High-Entropy Alloys) at Elevated Temperatures in Air. Adv. Eng. Mater. 2015, 17, 1134–1141.

- (18) Kai, W.; Li, C. C.; Cheng, F. P.; Chu, K. P.; Huang, R. T.; Tsay, L. W.; Kai, J. J. Air-Oxidation of Feconicr-Based Quinary High-Entropy Alloys at 700–900 °C. *Corros. Sci.* **2017**, *121*, 116–125.
- (19) Butler, T. M.; Weaver, M. L. Oxidation Behavior of Arc Melted Alcocrfeni Multi-Component High-Entropy Alloys. *J. Alloys Compd.* **2016**, *674*, 229–244.
- (20) Laplanche, G.; Volkert, U. F.; Eggeler, G.; George, E. P. Oxidation Behavior of the Crmnfeconi High-Entropy Alloy. *Oxid. Met.* **2016**, *85*, 629–645.
- (21) Gorr, B.; Azim, M.; Christ, H. J.; Mueller, T.; Schliephake, D.; Heilmaier, M. Phase Equilibria, Microstructure, and High Temperature Oxidation Resistance of Novel Refractory High-Entropy Alloys. *J. Alloys Compd.* **2015**, *624*, 270–278.
- (22) Kai, W.; Li, C. C.; Cheng, F. P.; Chu, K. P.; Huang, R. T.; Tsay, L. W.; Kai, J. J. The Oxidation Behavior of an Equimolar Feconicrmn High-Entropy Alloy at 950°C in Various Oxygen-Containing Atmospheres. *Corros. Sci.* **2016**, *108*, 209–214.
- (23) Xia, W.; Yang, Y.; Meng, Q.; Deng, Z.; Gong, M.; Wang, J.; Wang, D.; Zhu, Y.; Sun, L.; Xu, F.; Li, J.; Xin, H. L. Bimetallic Nanoparticle Oxidation in Three Dimensions by Chemically Sensitive Electron Tomography and *in Situ* Transmission Electron Microscopy. *ACS Nano* **2018**, *12*, 7866–7874.
- (24) Zhu, Y.; Sushko, P. V.; Melzer, D.; Jensen, E.; Kovarik, L.; Ophus, C.; Sanchez-Sanchez, M.; Lercher, J. A.; Browning, N. D. Formation of Oxygen Radical Sites on Movnbteox by Cooperative Electron Redistribution. *J. Am. Chem. Soc.* **2017**, *139*, 12342–12345.
- (25) Zou, L.; Li, J.; Zakharov, D.; Stach, E. A.; Zhou, G. *In Situ* Atomic-Scale Imaging of the Metal/Oxide Interfacial Transformation. *Nat. Commun.* **2017**, *8*, 307.
- (26) Wang, C.-M.; Genc, A.; Cheng, H.; Pullan, L.; Baer, D. R.; Bruemmer, S. M. *In-Situ* TEM Visualization of Vacancy Injection and Chemical Partition During Oxidation of Ni-Cr Nanoparticles. *Sci. Rep.* **2015**, *4*, 3683.
- (27) Jeangros, Q.; Hansen, T. W.; Wagner, J. B.; Damsgaard, C. D.; Dunin-Borkowski, R. E.; Hébert, C.; Van herle, J.; Hessler-Wyser, A. Reduction of Nickel Oxide Particles by Hydrogen Studied in an Environmental TEM. J. Mater. Sci. 2013, 48, 2893–2907.
- (28) Prestat, E.; Kulzick, M. A.; Dietrich, P. J.; Smith, M. M.; Tien, M. E. P.; Burke, M. G.; Haigh, S. J.; Zaluzec, N. J. *In Situ* Industrial Bimetallic Catalyst Characterization Using Scanning Transmission Electron Microscopy and X-Ray Absorption Spectroscopy at One Atmosphere and Elevated Temperature. *ChemPhysChem* **2017**, *18*, 2151–2156.
- (29) Xin, H. L.; Niu, K.; Alsem, D. H.; Zheng, H. *In Situ* TEM Study of Catalytic Nanoparticle Reactions in Atmospheric Pressure Gas Environment. *Microsc. Microanal.* **2013**, *19*, 1558–1568.
- (30) Jiang, Y.; Li, H.; Wu, Z.; Ye, W.; Zhang, H.; Wang, Y.; Sun, C.; Zhang, Z. *In Situ* Observation of Hydrogen-Induced Surface Faceting for Palladium—Copper Nanocrystals at Atmospheric Pressure. *Angew. Chem., Int. Ed.* **2016**, *55*, 12427—12430.
- (31) Dembélé, K.; Bahri, M.; Melinte, G.; Hirlimann, C.; Berliet, A.; Maury, S.; Gay, A. S.; Ersen, O. Insight by *in Situ* Gas Electron Microscopy on the Thermal Behaviour and Surface Reactivity of Cobalt Nanoparticles. *ChemCatChem* **2018**, *10*, 4004–4009.
- (32) Tan, S. F.; Chee, S. W.; Baraissov, Z.; Jin, H.; Tan, T. L.; Mirsaidov, U. Real-Time Imaging of Nanoscale Redox Reactions over Bimetallic Nanoparticles. *Adv. Funct. Mater.* **2019**, *29*, 1903242.
- (33) Altantzis, T.; Lobato, I.; De Backer, A.; Béché, A.; Zhang, Y.; Basak, S.; Porcu, M.; Xu, Q.; Sánchez-Iglesias, A.; Liz-Marzán, L. M.; Van Tendeloo, G.; Van Aert, S.; Bals, S. Three-Dimensional Quantification of the Facet Evolution of Pt Nanoparticles in a Variable Gaseous Environment. *Nano Lett.* **2019**, *19*, 477–481.
- (34) Song, B.; Yang, T. T.; Yuan, Y.; Sharifi-Asl, S.; Cheng, M.; Saidi, W. A.; Liu, Y.; Shahbazian-Yassar, R. Revealing Sintering Kinetics of MoS₂-Supported Metal Nanocatalysts in Atmospheric Gas Environments *via* Operando Transmission Electron Microscopy. *ACS Nano* **2020**, *14*, 4074–4086.
- (35) Li, Y.; Zakharov, D.; Zhao, S.; Tappero, R.; Jung, U.; Elsen, A.; Baumann, P.; Nuzzo, R. G.; Stach, E. A.; Frenkel, A. I. Complex

- Structural Dynamics of Nanocatalysts Revealed in Operando Conditions by Correlated Imaging and Spectroscopy Probes. *Nat. Commun.* **2015**, *6*, 7583.
- (36) Wu, Y. A.; Li, L.; Li, Z.; Kinaci, A.; Chan, M. K.; Sun, Y.; Guest, J. R.; McNulty, I.; Rajh, T.; Liu, Y. Visualizing Redox Dynamics of a Single Ag/AgCl Heterogeneous Nanocatalyst at Atomic Resolution. *ACS Nano* **2016**, *10*, 3738–3746.
- (37) Han, L.; Meng, Q.; Wang, D.; Zhu, Y.; Wang, J.; Du, X.; Stach, E. A.; Xin, H. L. Interrogation of Bimetallic Particle Oxidation in Three Dimensions at the Nanoscale. *Nat. Commun.* **2016**, *7*, 13335.
- (38) Wagner, C. Beitrag Zur Theorie Des Anlaufvorgangs. Z. Phys. Chem. 1933, 21, 25-41.
- (39) Zhdanov, V. P.; Kasemo, B. Cabrera—Mott Kinetics of Oxidation of nm-Sized Metal Particles. *Chem. Phys. Lett.* **2008**, 452, 285–288.
- (40) Miley, H. A. Theory of Oxidation and Tarnishing of Metals. *Trans. Electrochem. Soc.* **1942**, *81*, 391.
- (41) Henz, B. J.; Hawa, T.; Zachariah, M. R. On the Role of Built-in Electric Fields on the Ignition of Oxide Coated Nanoaluminum: Ion Mobility *versus* Fickian Diffusion. *J. Appl. Phys.* **2010**, *107*, 024901.
- (42) Anderson, B. D.; Tracy, J. B. Nanoparticle Conversion Chemistry: Kirkendall Effect, Galvanic Exchange, and Anion Exchange. *Nanoscale* **2014**, *6*, 12195–12216.
- (43) Grammatikopoulos, P.; Sowwan, M.; Kioseoglou, J. Computational Modeling of Nanoparticle Coalescence. *Advanced Theory and Simulations* **2019**, *2*, 1900013.
- (44) Rai, A.; Park, K.; Zhou, L.; Zachariah, M. R. Understanding the Mechanism of Aluminium Nanoparticle Oxidation. *Combust. Theory Modell.* **2006**, *10*, 843–859.
- (45) Chen, Y.; Zhao, X.; Xiao, P. Effect of Surface Curvature on Oxidation of a Mcraly Coating. *Corros. Sci.* **2020**, *163*, 108256.
- (46) Laplanche, G.; Kostka, A.; Reinhart, C.; Hunfeld, J.; Eggeler, G.; George, E. P. Reasons for the Superior Mechanical Properties of Medium-Entropy Crconi Compared to High-Entropy Crmnfeconi. *Acta Mater.* **2017**, *128*, 292–303.
- (47) Chen, S.; Oh, H. S.; Gludovatz, B.; Kim, S. J.; Park, E. S.; Zhang, Z.; Ritchie, R. O.; Yu, Q. Real-Time Observations of Trip-Induced Ultrahigh Strain Hardening in a Dual-Phase Crmnfeconi High-Entropy Alloy. *Nat. Commun.* **2020**, *11*, 826.
- (48) Ahn, C. C.; Krivanek, O. L. EELS Atlas: A Reference Guide of Electron Energy Loss Spectra Covering All Stable Elements; ASU HREM Facility & Gatan Inc.: Warrendale, PA, 1983; pp 1–92.
- (49) Ewels, P.; Sikora, T.; Serin, V.; Ewels, C. P.; Lajaunie, L. A Complete Overhaul of the Electron Energy-Loss Spectroscopy and X-Ray Absorption Spectroscopy Database: Eelsdb.Eu. *Microsc. Microanal.* **2016**, *22*, 717–724.
- (50) Feldhoff, A.; Martynczuk, J.; Arnold, M.; Myndyk, M.; Bergmann, I.; Šepelák, V.; Gruner, W.; Vogt, U.; Hähnel, A.; Woltersdorf, J. Spin-State Transition of Iron in (Ba_{0.5}Sr_{0.5})(Fe_{0.8}Zn_{0.2})-O₃-Δ Perovskite. *J. Solid State Chem.* **2009**, *182*, 2961–2971.
- (51) Zhao, Y.; Feltes, T. E.; Regalbuto, J. R.; Meyer, R. J.; Klie, R. F. *In Situ* Electron Energy Loss Spectroscopy Study of Metallic Co and Co Oxides. *J. Appl. Phys.* **2010**, *108*, 063704.
- (52) Potapov, P. L.; Kulkova, S. E.; Schryvers, D.; Verbeeck, J. Structural and Chemical Effects on EELS L_{3,2} Ionization Edges in Ni-Based Intermetallic Compounds. *Phys. Rev. B: Condens. Matter Mater. Phys.* **2001**, *64*, 184110.
- (53) Ngantcha, J. P.; Gerland, M.; Kihn, Y.; Rivière, A. Correlation between Microstructure and Mechanical Spectroscopy of a Cu-Cu₂O Alloy between 290 and 873 K. Eur. Phys. J.: Appl. Phys. **2005**, 29, 83–89.
- (54) Guo, J.; Haberfehlner, G.; Rosalie, J.; Li, L.; Duarte, M. J.; Kothleitner, G.; Dehm, G.; He, Y.; Pippan, R.; Zhang, Z. *In Situ* Atomic-Scale Observation of Oxidation and Decomposition Processes in Nanocrystalline Alloys. *Nat. Commun.* **2018**, *9*, 946.
- (55) Wang, F.; Malac, M.; Egerton, R. F. Energy-Loss Near-Edge Fine Structures of Iron Nanoparticles. *Micron* **2006**, *37*, 316–323.
- (56) Wang, Z. L.; Yin, J. S.; Jiang, Y. D. EELS Analysis of Cation Valence States and Oxygen Vacancies in Magnetic Oxides. *Micron* **2000**, *31*, 571–580.

- (57) Wang, Z. L.; Yin, J. S.; Mo, W. D.; Zhang, Z. J. *In-Situ* Analysis of Valence Conversion in Transition Metal Oxides Using Electron Energy-Loss Spectroscopy. *J. Phys. Chem. B* **1997**, *101*, 6793–6798.
- (58) Varela, M.; Oxley, M. P.; Luo, W.; Tao, J.; Watanabe, M.; Lupini, A. R.; Pantelides, S. T.; Pennycook, S. J. Atomic-Resolution Imaging of Oxidation States in Manganites. *Phys. Rev. B: Condens. Matter Mater. Phys.* **2009**, *79*, 085117.
- (59) Jeurgens, L. P. H.; Sloof, W. G.; Tichelaar, F. D.; Mittemeijer, E. J. Thermodynamic Stability of Amorphous Oxide Films on Metals: Application to Aluminum Oxide Films on Aluminum Substrates. *Phys. Rev. B: Condens. Matter Mater. Phys.* **2000**, *62*, 4707–4719.
- (60) Fehlner, F. P. Low Temperature Oxidation, the Role of Vitreous Oxides; Wiley-Interscience: Hoboken, NJ, 1986.
- (61) Cabrera, N.; Mott, N. F. Theory of the Oxidation of Metals. *Rep. Prog. Phys.* **1949**, *12*, 163–184.
- (62) Jiang, N. Electron Beam Damage in Oxides: A Review. Rep. Prog. Phys. 2016, 79, 016501.
- (63) Zhang, D.; Jin, C.; Tian, H.; Xiong, Y.; Zhang, H.; Qiao, P.; Fan, J.; Zhang, Z.; Li, Z. Y.; Li, J. An *in Situ* TEM Study of the Surface Oxidation of Palladium Nanocrystals Assisted by Electron Irradiation. *Nanoscale* **2017**, *9*, 6327–6333.
- (64) Purton, J. A.; Barrera, G. D.; Allan, N. L.; Blundy, J. D. Monte Carlo and Hybrid Monte Carlo/Molecular Dynamics Approaches to Order- Disorder in Alloys, Oxides, and Silicates. *J. Phys. Chem. B* **1998**, 102, 5202–5207.
- (65) Widom, M.; Huhn, W. P.; Maiti, S.; Steurer, W. Hybrid Monte Carlo/Molecular Dynamics Simulation of a Refractory Metal High Entropy Alloy. *Metall. Mater. Trans. A* **2014**, *45*, 196–200.
- (66) Zhu, Q.; Zou, L.; Zhou, G.; Saidi, W. A.; Yang, J. C. Early and Transient Stages of Cu Oxidation: Atomistic Insights from Theoretical Simulations and *in Situ* Experiments. *Surf. Sci.* **2016**, *652*, 98–113.
- (67) Curnan, M. T.; Andolina, C. M.; Li, M.; Zhu, Q.; Chi, H.; Saidi, W. A.; Yang, J. C. Connecting Oxide Nucleation and Growth to Oxygen Diffusion Energetics on Stepped Cu(011) Surfaces: An Experimental and Theoretical Study. *J. Phys. Chem. C* **2019**, *123*, 452–463.
- (68) Saidi, W. A.; Lee, M.; Li, L.; Zhou, G.; McGaughey, A. J. H. *Ab Initio* Atomistic Thermodynamics Study of the Early Stages of Cu(100) Oxidation. *Phys. Rev. B: Condens. Matter Mater. Phys.* **2012**, 86, 245429.
- (69) Zhu, Q.; Saidi, W. A.; Yang, J. C. Step-Edge Directed Metal Oxidation. J. Phys. Chem. Lett. 2016, 7, 2530–2536.
- (70) Vitos, L.; Ruban, A. V.; Skriver, H. L.; Kollár, J. The Surface Energy of Metals. *Surf. Sci.* **1998**, *411*, 186–202.
- (71) Perdew, J. P.; Burke, K.; Ernzerhof, M. Generalized Gradient Approximation Made Simple. *Phys. Rev. Lett.* **1996**, *77*, 3865–3868.
- (72) Kresse, G.; Hafner, J. Ab Initio Molecular Dynamics for Liquid Metals. Phys. Rev. B: Condens. Matter Mater. Phys. 1993, 47, 558.
- (73) Kresse, G.; Hafner, J. Ab Initio Molecular Dynamics for Open-Shell Transition Metals. Phys. Rev. B: Condens. Matter Mater. Phys. 1993, 48, 13115.
- (74) Kresse, G.; Hafner, J. *Ab Initio* Molecular-Dynamics Simulation of the Liquid-Metal-Amorphous-Semiconductor Transition in Germanium. *Phys. Rev. B: Condens. Matter Mater. Phys.* **1994**, 49, 14251.
- (75) Kresse, G.; Joubert, D. From Ultrasoft Pseudopotentials to the Projector Augmented-Wave Method. *Phys. Rev. B: Condens. Matter Mater. Phys.* **1999**, 59, 1758–1775.
- (76) Goedecker, S.; Teter, M.; Hutter, J. Separable Dual-Space Gaussian Pseudopotentials. *Phys. Rev. B: Condens. Matter Mater. Phys.* **1996**, *54*, 1703–1710.
- (77) VandeVondele, J.; Krack, M.; Mohamed, F.; Parrinello, M.; Chassaing, T.; Hutter, J. Quickstep: Fast and Accurate Density Functional Calculations Using a Mixed Gaussian and Plane Waves Approach. *Comput. Phys. Commun.* **2005**, *167*, 103–128.